Christopher Hendricks[1]
Center for Advanced Life Cycle Engineering (CALCE),
University of Maryland,
College Park, MD 20817;
Naval Surface Warfare Center,
West Bethesda, MD 20817
e-mail: christopher.e.hendricks4.civ@us.navy.mil

Bhanu Sood
Quality and Reliability Division,
Safety and Mission Assurance Directorate,
NASA Goddard Space Flight Center,
Greenbelt, MD 20771
e-mail: bhanu.sood@nasa.gov

Michael Pecht
Center for Advanced Life Cycle Engineering (CALCE),
University of Maryland,
College Park, MD 20742
e-mail: pecht@umd.edu

Lithium-Ion Battery Strain Gauge Monitoring and Depth of Discharge Estimation

Lithium-ion battery diagnostics and prognostics rely on measurements of electrical impedance, capacity, and voltage to infer the internal state of the battery. Mechanical changes to the cell structure represent an additional measure of the battery's state because these changes are related to the overall battery health. As lithium-ion batteries are charged and discharged, lithium ions are inserted or removed from the anode and cathode, a process called intercalation and deintercalation. As lithium ions intercalate and de-intercalate, they can cause changes to the lattice of the electrode particles, resulting in volumetric changes. These volumetric changes cause mechanical stresses and strains on the lithium-ion battery electrodes, and subsequently, the whole cell's thickness varies as it is charged and discharged. This paper presents a study on the use of surface-mounted strain gauges for in-situ measurement of structural changes to lithium-ion batteries, along with a characterization of the unit-to-unit differences in strain response. A neural network modeling structure is then used to predict the battery's depth of discharge under dynamic discharge conditions. [DOI: 10.1115/1.4054340]

Keywords: lithium-ion batteries, depth of discharge, strain gauges, neural networks

1 Introduction

Lithium-ion batteries are emerging as the battery of choice for a wide range of applications. Due to their high-energy density, absence of a "memory" effect, and high voltage potential, lithium-ion batteries are increasingly seeing use in industrial applications including uninterruptible power supplies and large-scale grid storage. Despite their widespread use, lithium-ion batteries present unique control and safety challenges. These challenges can be addressed through improved design, control, and innovative sensing technologies.

Lithium-ion batteries experience volumetric changes as lithium ions intercalate and de-intercalate into and out of the electrode particles [1–11]. The intercalation and deintercalation are accompanied by expansion and contraction of the call. As a result of expansion and contraction of particles, stresses act on the composite electrodes, resulting in thickness changes on the overall cell level [12–31]. The thickness changes, in turn, cause tensile and compressive stresses to be placed on the external casing, which results in strain. This multi-scale effect is illustrated in Fig. 1.

The amount of expansion is partially based on the material's ability to accommodate lithium ions in its lattice structure. Lithium cobalt oxide ($LiCoO_2$) expands as lithium ions are removed from its structure due to the repulsion of CoO_2 layers [1]. Variations of doped $LiCoO_2$ also exhibit this behavior [5]. Alternately, cathodes composed of lithium iron phosphate ($LiFePO_4$) contract by approximately 6.5% as lithium is removed [6]. Lithium manganese dioxide ($LiMn_2O_4$) undergoes structural changes as lithium ions are added and removed from its spinel structure [7]. Graphite is the main contributor to depth of discharge (DOD)-dependent swelling in conventional lithium-ion cells. Graphite experiences an approximate 10% volume change as lithium ions are inserted between its layered sheets as identified through X-ray diffraction [8,9].

In addition to monitoring lattice-level changes in lithium-ion cell electrode materials, researchers have investigated the swelling effect of lithium-ion cells and battery packs. This has been accomplished using optical observation [10,11], load cells [12–18], linear voltage displacement transducers [19–24], fiber Bragg grating sensors [25], ultrasonic transducers [26–28], high-energy X-ray diffraction [29], and multidimensional laser scanning [30]. Many of the studies were conducted to look at a single cell without examining either unit-to-unit differences or the full pack force which cannot discriminate between cells. There is variability in the cell's expansion and contraction behavior based on the chemistry of each electrode, electrode geometry (wound vs. stacked electrodes), cell mechanical constraints, temperature, and rate of charge or discharge. Derivatives of thickness changes [21] have been shown to mimic incremental capacity curves (dV/dQ and dQ/dV, where V is voltage, and Q is capacity), which allows for the extraction of state of charge (SOC)- and state of health (SOH)-related information.

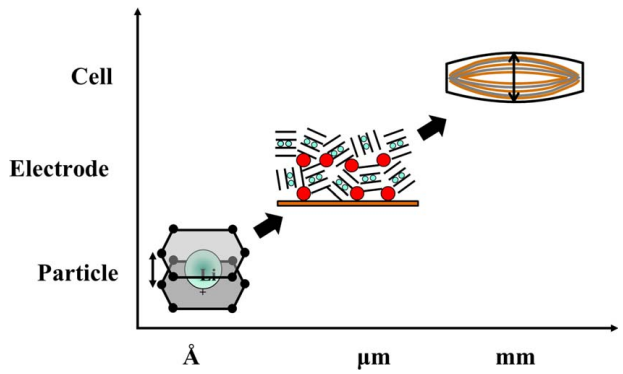

Fig. 1 Multi-scale effect of lithium-ion intercalation

[1]Corresponding author.

Manuscript received December 1, 2021; final manuscript received April 11, 2022; published online May 12, 2022. Assoc. Editor: Corey T. Love.

Changes in cell thickness or casing strain can also be attributed to internal processes related to cell formation, aging, and abuse as a result of gas generation and swelling. Depending on when strain or thickness is monitored, these effects may or may not play a role in the baseline strain or thickness measurement. For short-term cycling behavior, the contributions of gas generation can be neglected; however, it is expected to add to the baseline strain measured as the battery ages or undergoes an abusive event.

Physics-based models have been developed [16,20,23] that can capture the coupled thermal–mechanical–electrochemical interactions of the cell; however, these models are often not practical for real-time applications unless the model reduction is performed, and they require measurement of a large number of physical properties of the cell and its materials. Furthermore, the model will not be able to adequately handle unit-to-unit differences that arise due to manufacturing variability. The variability originates from specific design characteristics, materials, and processes used for the fabrication. Finally, phenomenological models [14,16,18] have been proposed that model the forces a cell or battery pack exerts on a load cell as it expands and contracts. The bulk force of a pack does not capture individual cell responses, and therefore does not capture cell imbalances or unit-to-unit differences.

Researchers have studied thickness changes in lithium-ion cells, and some efforts have been made to incorporate mechanical effects into physics-based models. The majority of the approaches reported require rigid fixtures and sensitive displacement transducers or load cells to measure cell expansion. Finally, the papers do not address the impact of unit-to-unit variability on the mechanical response of the cell. A more practical approach involving surface-mount strain gauges to measure mechanical changes is presented in this paper. A data-driven model is utilized to capture unit-to-unit differences and nonlinear interactions between strain and state of charge.

2 Depth of Discharge Estimation

Many methods already exist for DOD estimations. Extensive reviews of prognostic and diagnostic methods and algorithms have been performed by Zhang and Lee [32], Piller et al. [33], and Saha et al. [34]. One of the most prevalent methods for tracking the amount of charge in a battery is through coulomb counting [34,36] If the initial DOD is unknown, or if the battery undergoes complex charge and discharge cycles, coulomb counting can introduce errors and inaccuracies. Additionally, coulomb counting values can drift over time due to measurement noise, and they often need recalibration. In laboratory-based studies, however, coulomb counting can be used as the "true" DOD value. Coulomb counting is the standard against which the neural network model in this paper is compared.

In practical lithium-ion battery applications, DOD can also be estimated through a variety of models that relate measured parameters such as voltage and temperature to the DOD. These approaches include equivalent circuit models (ECMs), black-box models (e.g., neural networks, support vector machines, and autoregressive integrated moving average), and electrochemical models [32–42]. Any of these types of models can be combined with a filter (e.g., Kalman Filter) to provide a feedback loop and error cancellation [42].

In this work, a feedforward neural network (NN) structure used for regression was used to relate measurements of strain (input) to the depth of discharge (output). Its general structure can be seen in Fig. 2. The structure consists of a set of inputs, labeled ε_1 through ε_n. These represent strain measurements covering the full range of the depth of discharge, with the length of the vector determined based upon the sampling rate and the time required to reach the end of discharge voltage. A bias term is a constant that is not influenced by the previous layer and is analogous to the y-intercept in a linear regression problem. The neural network was trained using known, labeled data to establish the proper weights, W, for the neuron connections by calculating DOD using the Coloumb counting method.

Although a filtering methodology can be applied to further reduce error, the baseline model error is assessed to determine the extent to

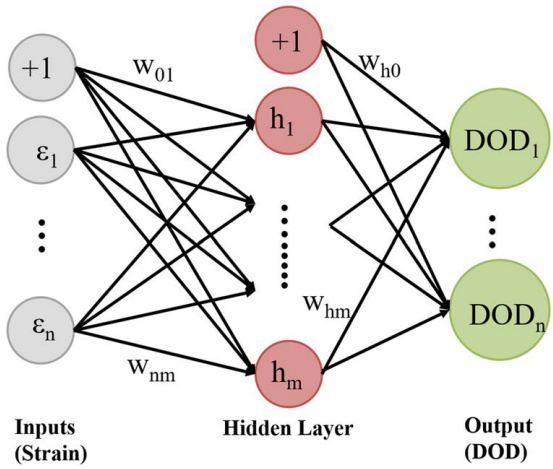

Fig. 2 Neural network for prediction of depth of discharge from input strain measurements

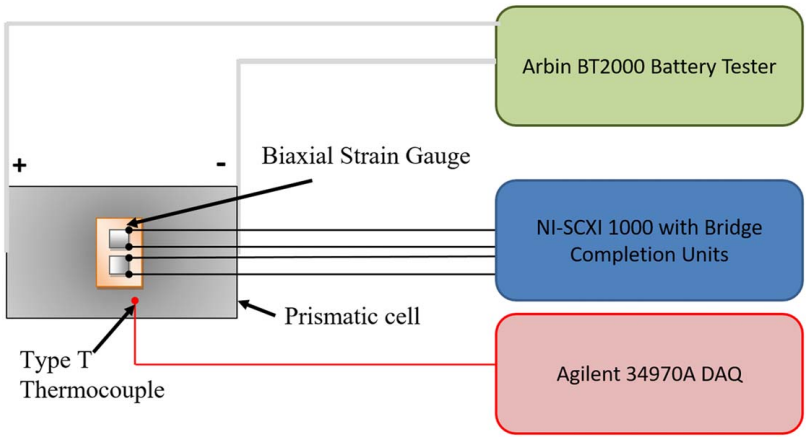

Fig. 3 Experimental setup with strain gauge monitoring

Table 1 Test protocol for collecting training and test data

Test	Test description
C/5 cycling	One cycle with C/5 charge and discharge rates
C/2 cycling	Five cycles with C/2 charge and discharge rates
Federal urban driving schedule	One cycle with a dynamic discharge profile repeated until cell voltage reaches 3.0 V
C/2 cycling	One cycle with C/2 charge and discharge rates
Federal urban driving schedule	One cycle with a dynamic discharge profile repeated until cell voltage reaches 3.0 V

which strain can be used to predict DOD in the absence of voltage measurement. The Neural Network Toolbox (version 11.0) in MATLAB will be applied to build the neural network model structure and train the model.

3 Experimental

Tests were performed on prismatic lithium-ion cells with a nominal capacity of 1.10 Ah and dimensions 48.6 mm × 33.8 mm × 6.1 mm. Four cells were used in the study and were tested in an

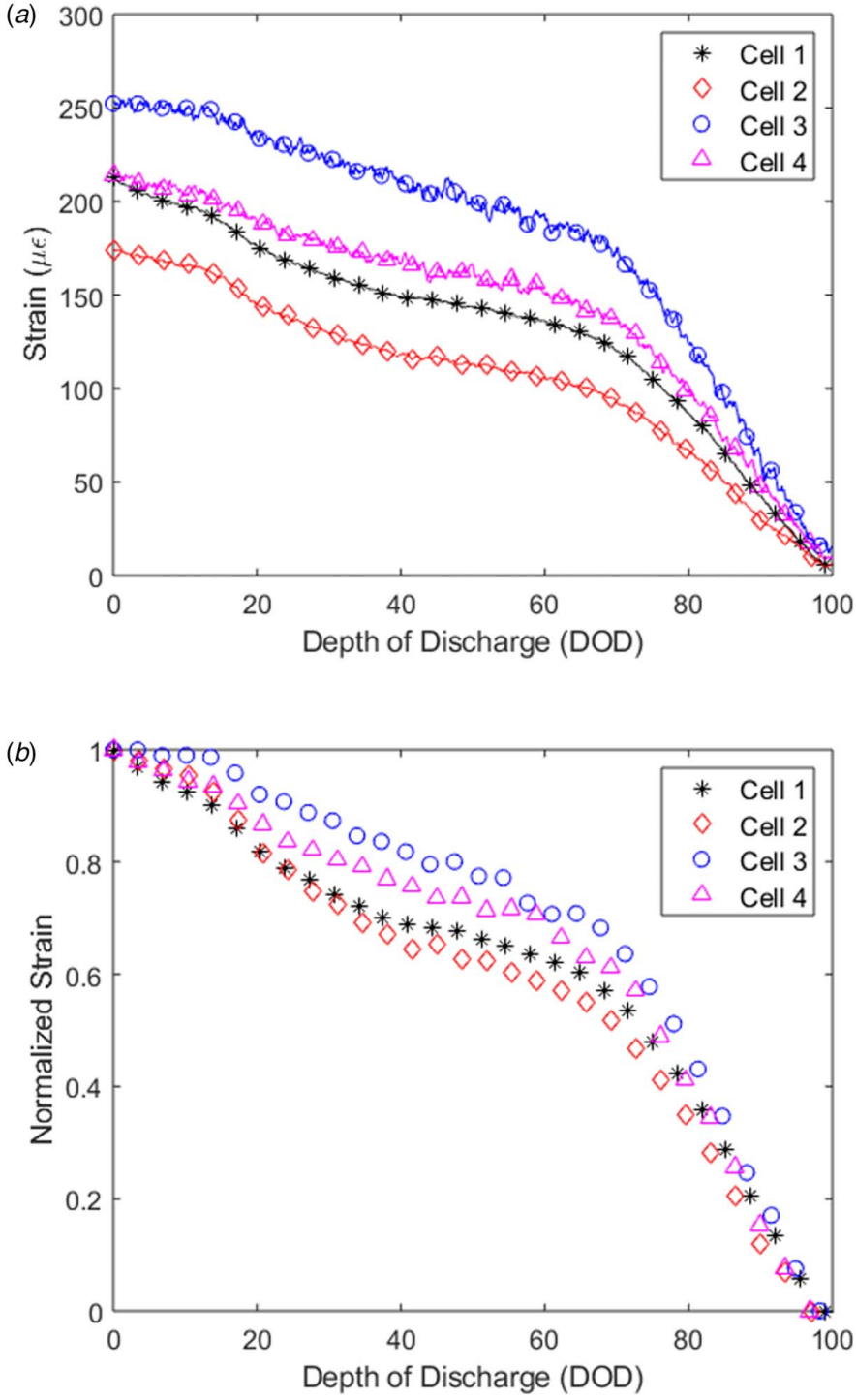

Fig. 4 (*a*) Strain gauge measurements for four cells discharged at C/5 and (*b*) normalized strain gauge measurement at C/5 discharge rate

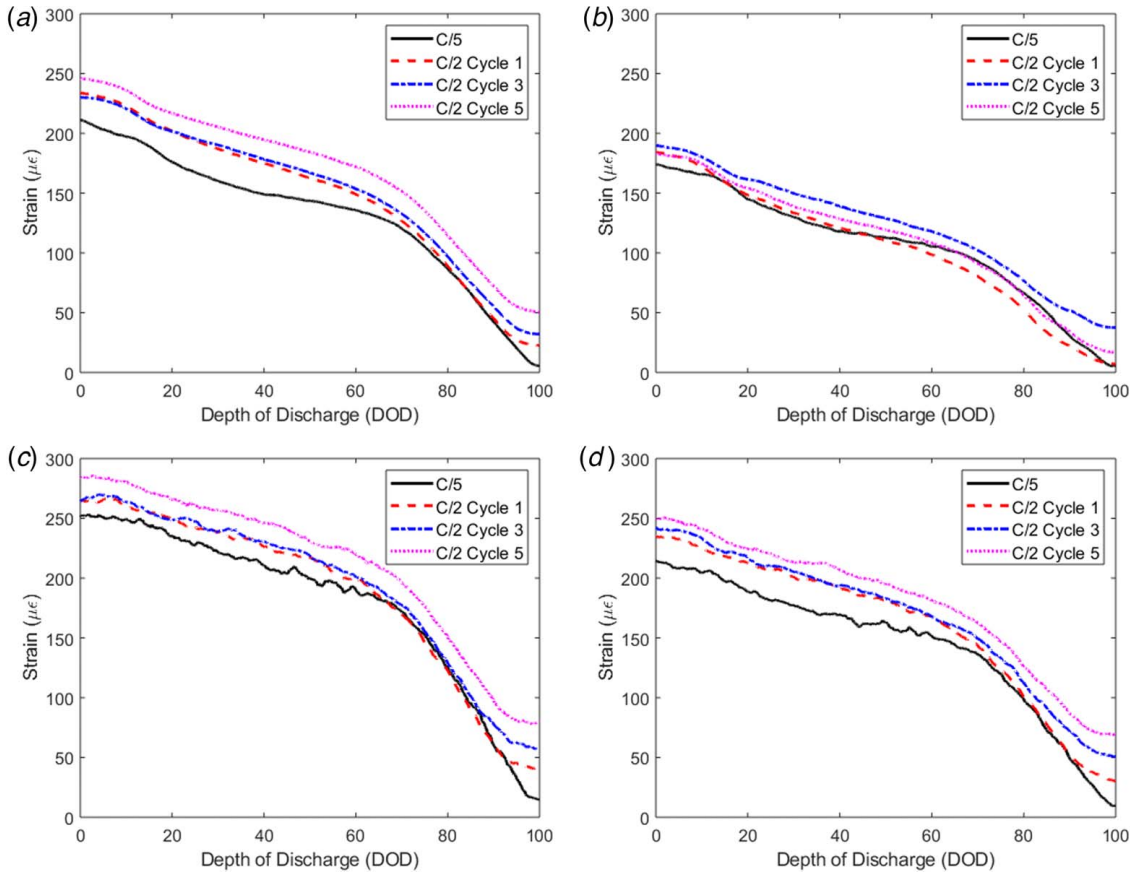

Fig. 5 Strain gauge measurements for (*a*) Cell 1, (*b*) Cell 2, (*c*) Cell 3, and (*d*) Cell 4 over several cycles

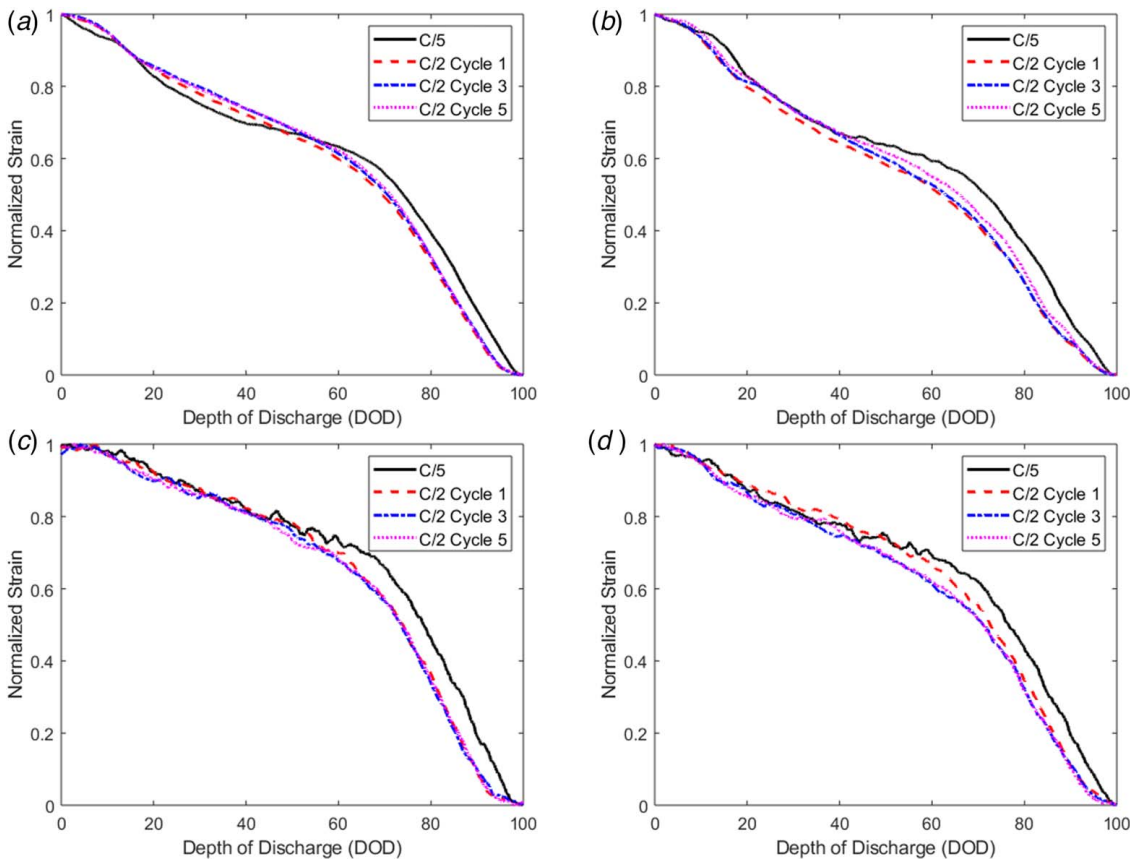

Fig. 6 Normalized strain gauge measurements for (*a*) Cell 1, (*b*) Cell 2, (*c*) Cell 3, and (*d*) Cell 4

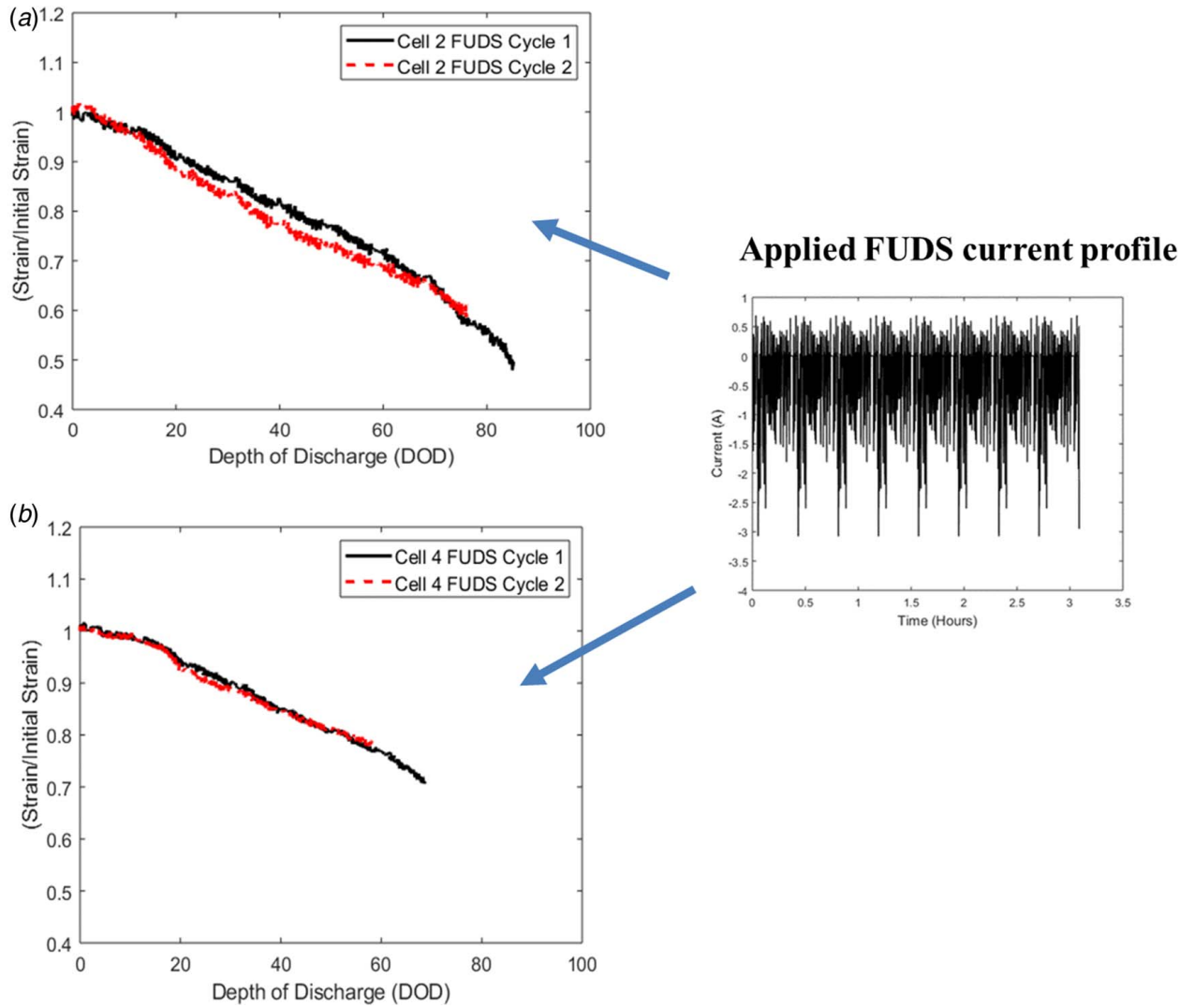

Fig. 7 FUDS Cycle 1 and Cycle 2 for (*a*) Cell 2 and (*b*) Cell 4

unconstrained configuration in a lab environment with an average temperature of 24 ± 4 °C. Charge/discharge cycling was performed on an Arbin BT2000 commercial battery tester. To measure the mechanical changes to the cell casing, 350 mΩ biaxial metal foil strain gauges obtained from Omega Engineering (part # KFH-3-350-D16-11L3M3S) were attached to the outer casing of a cell using an ethyl-based cyanoacrylate adhesive (part # SG496). Prior to adhering the strain gauge to the cell casing, the cell casing was prepared by removing surface contaminants with sandpaper and cleaning with acetone. The strain gauge was mounted in the center of the cell where the maximum strain should occur due to the wound nature of the electrode jelly roll. The strain was monitored using a National Instruments SCXI-1000 data acquisition unit with an SCXI-1520 bridge-completion board, and the cell-casing temperature was monitored using a Type-T thermocouple and an Agilent 34970A data logger. The thermocouple was mounted on the surface of the casing. The experimental setup is schematically shown in Fig. 3.

The strain was measured utilizing a half-bridge I configuration, which provides temperature compensation by monitoring strain in both of the strain gauge patterns on the cell. The strain gauge cables were shortened to 1 m long to minimize resistive contributions from the wire. The strain was calibrated and zeroed prior to the start of testing using National Instruments NI-Max software. The primary strain direction was chosen as the width-wise direction. Changes due entirely to temperature are measured in the second strain direction and subtracted from the overall response seen in the primary strain direction. In this manner, the strain measured is related to the mechanical changes to the cell and not due to fluctuations in the ambient or surface temperature of the cell. Thermal expansion of the internal cell components, however, will contribute to the mechanical strain measured in the half-bridge I configuration. Strain measurements were captured at a frequency of 0.1 Hz with an excitation voltage of 5 V. Charging was performed using a constant current/constant voltage charge profile. The constant voltage portion of the charging profile was initiated when the cell's voltage reached 4.20 Volts and terminated when the charge current decayed below a C-rate of C/10. Discharging was performed at C/5 and C/2 discharge rates. The cells were also tested using the Federal Urban Driving Schedule (FUDS) profile scaled for an 1100 mAh cell. A summary of the tests conducted is given in Table 1.

4 Results and Discussion

External measurements of strain can be attributed to a number of factors over both the short and long term. Short-term strain fluctuations can be due to intercalation/deintercalation of lithium from the active materials in the electrodes, changes in ambient temperature, thermal expansion of the cell components, changes in external pressure or loading, or the sudden generation of gas inside of the cell

due to an abusive operating condition. Long-term changes in strain can be attributed to thickening of the electrodes, electrode buckling, and progressive gas generation due to side reactions associated with aging mechanisms (solid electrolyte interphase (SEI) layer growth). To distinguish between long-term and short-term changes in strain, a number of methods were employed including the use of a half-bridge configuration to minimize the effect of purely temperature-induced strain. Furthermore, the battery was maintained within its recommended operating temperature, current, and voltage to avoid abusive operating conditions. The cells were cycled and their capacity monitored to ensure that the formation process was already complete and to reduce the influence of gas generation on the measured strain response. Finally, a limited number of tests were conducted to minimize the contributions of long-term changes to the cell.

To minimize the noise in the signal, a 10-point moving average of the strain data was taken using the Matlab function *movmean* and plotted in Fig. 4(*a*). Unit-to-unit differences are apparent in the raw strain data; however, the cells are all within the same order of magnitude with a change in strain of 175–250 $\mu\varepsilon$ from the start of discharge (0% DOD) to the end of discharge (100% DOD). The cells also have an overall similar trend in the strain as a function of DOD. Due to the nature of the external strain measurement, this result is expected. Unit-to-unit differences exist in lithium-ion batteries when measuring capacity and impedance, and the strain resulting from intercalation-induced electrode stresses behaves similarly. Due to the random orientation of active material particles and heterogeneous nature of the composite electrode, variations in cell swelling magnitude during charge and discharge will occur and subsequently lead to different casing strain responses. When the strain response is normalized and plotted, the four cells exhibit similar behavior; however, variation exists in the middle region of the discharge (between 30% and 60% DOD) as shown in Fig. 4(*b*).

After the C/5 charge and discharge cycle, five cycles are performed at a higher C-rate of C/2 as shown in Fig. 5. The strain curve begins shifting upward with subsequent cycles for all but one cell, Cell 2. If the curves are normalized as shown in Fig. 6, the C/2 curves largely overlap with the C/5 curve; however, some detail is lost in the curve as a result of the higher discharge rate. Particularly for Cell 1 and Cell 2, inflections in the strain curve become more pronounced at a slower discharge rate. In Ref. [10], inflection points in the discharge curve are attributed to stage transitions in the graphite. As graphite undergoes the largest dimensional changes during intercalation compared to $LiCoO_2$, it is clear that dimensional changes to graphite will dominate the overall mechanical response of the cell.

The dynamic response of the strain gauge was assessed by discharging the cell using the FUDS current profile shown to the right in Fig. 7. The profile was repeated until the cell reached the lower voltage cutoff of 3.0 V. This often occurred before the battery's capacity was fully depleted due to a high current pulse polarizing the cell and reaching the safety cutoff. The two FUDS cycles for Cell 2 and Cell 4 are shown in Figs. 7(*a*) and 7(*b*), respectively.

The Neural Network Toolbox (version 11.0) in Matlab was used to build the neural network model structure and train the model. The neural network framework chosen was a feedforward neural network with a hidden layer and an output layer. The strain measurements were taken as inputs, and the output is an estimated DOD value. Although sampling of strain was conducted at 0.1 Hz, the battery test equipment was logged at 1 Hz. Therefore, a subset of the strain data was selected corresponding to the time-stamps of the voltage and current data. The total number of strain and DOD data points was 12,500 for Cell 2 and 9900 for Cell 4. Ten-fold cross-validation was used to separate the full data set into ten different partitions. The model was trained on nine partitions using the Levenberg–Marquardt backpropagation method and tested using the remaining partition of data. This process is repeated nine additional times, leaving out a different partition for test data each time. At each iteration, the performance of the model is evaluated by calculating the mean square error between the estimated DOD and the true DOD values. The average performance over the whole data set can then be calculated and used to vary additional model parameters. To determine the number of neurons within the hidden layer, the 10-fold cross-validation procedure was performed for networks with 1–10 neurons in the hidden layer. The average model error did not decrease significantly beyond five neurons in the hidden layer; therefore, the model was built using five neurons in the hidden layer. The model was trained on the first FUDS cycle and tested using the second FUDS cycle. The results of the model fit for Cells 2 and 4 are shown in Figs. 8(*a*) and 8(*b*), respectively. The predicted DOD based solely on strain gauge measurements tracks the true DOD well, with a mean square error of 2.4×10^{-3} for cell 2 and 5.59×10^{-4} for cell 4.

The predicted depth of discharge using strain values as inputs is very accurate even for dynamic discharge data. During the intermediate DOD range between 20% and 60%, the predicted depth of discharge tends to overestimate compared to the true state. This effect is more pronounced in cell 2; however, the raw strain data demonstrated more variability as well. Additional FUDS cycles were not conducted, but future model implementations would need to account for long-term changes to strain due to aging effects and may be able to reduce error further to make the model more

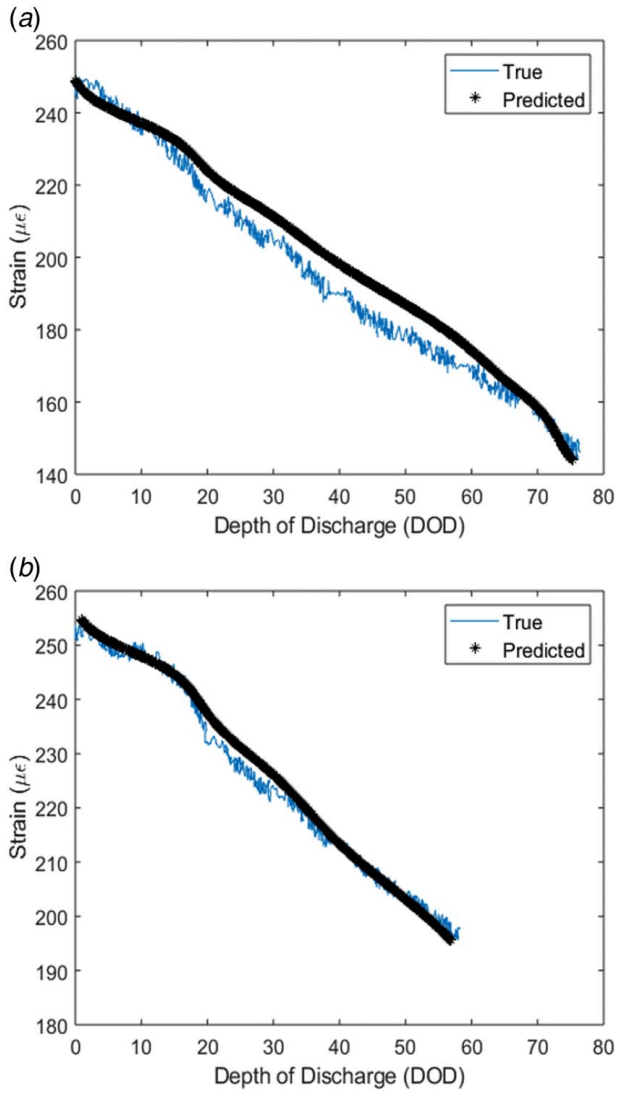

Fig. 8 Neural network prediction of FUDS data for (*a*) Cell 2 and (*b*) Cell 4

generalizable. While additional data could be collected for many cycles and used to build the neural network model, the inherent cycle-to-cycle differences in strain response will result in some level of error. For a cell in which the strain response does not change significantly over the short term, such as Cell 4, the model accuracy is very good. For a cell in which the strain response changes from cycle to cycle, errors could be greater; however, the overall change in DOD is still captured. These cycle-to-cycle changes are inevitable as continual expansion/contraction of the cell can lead to electrode buckling. Furthermore, the growth of SEI and generation of gas over the life cycle of the battery will occur as well. As with a model that needs to take into account capacity fade in the prediction of DOD, the neural network will need additional inputs to account for battery aging and long-term mechanical changes to the battery's internal structure. The utility of strain measurements to predict battery DOD is very promising for a wide range of dynamic battery applications, as long as aging effects are taken into account.

5 Conclusions

The integration of sensors within a battery pack will help usher in a new era of battery management. Strain gauges offer a means of probing the battery's state in a non-intrusive manner and can be integrated into a battery system for diagnostic and prognostic purposes. The use of strain gauges to determine the health and safety of a battery system without stimulating the battery electrochemically is a tremendous benefit.

Depth of discharge estimation for lithium-ion batteries depends on models that can relate measureable signals to the battery's internal electrochemical state. In this paper, mechanical measurement of the cell-casing strain due to changes in cell thickness was examined. The mechanical measurement was evaluated for effectiveness in DOD estimation. Intercalation-induced stresses were detectable using surface-mounted strain gauges and correlated well with DOD. As the battery was charged, the strain increased, and when the battery was discharged (and DOD increased), the strain measurement decreased. The strain was able to track the overall cell depth of discharge, even under dynamic discharge conditions. Unit-to-unit differences in the mechanical response of different cells are apparent, but the cell strain measurements still follow similar trends. These differences necessitate that cells are well matched for their mechanical response as well as traditionally matched characteristics such as impedance or capacity.

Traditional DOD estimation relies on voltage, current, and temperature measurements; however, these methods do not account for the intercalation stresses. The use of strain has a number of benefits. While the cells tested in this study were lithium cobalt oxide ($LiCoO_2$), lithium iron phosphate ($LiFePO_4$) cells have a characteristically flat voltage profile over a wide range of DOD. As a result, purely voltage-based DOD estimation is prone to errors due to inaccurate current and voltage measurements. Therefore, the addition of strain gauges to a $LiFePO_4$-based battery will improve DOD estimation accuracy because the change in strain is more pronounced as a function of DOD due to the role of graphite in intercalation-induced stresses.

Strain gauges have an added application in battery health tracking, especially to identify anomalous behavior (e.g., when the strain measurements deviate from the model estimate), indicating the generation of unexpected levels of gas within the cell casing. Additional research correlating permanent changes to strain to internal cell processes including aging (electrode thickening and typical gas generation) and abuse (gas generated due to thermally- and electrochemically induced gas generation) will make the prospect of strain-based battery diagnostics more appealing. Monitoring strain would allow for the identification of anomalous cells in a large battery pack consisting of cells in parallel and series. In large battery arrays, anomaly detection by voltage alone can be challenging, and the addition of strain to not only detect an anomaly, but identify which cell has an anomaly is of tremendous benefit to battery safety. A model based on nonlinear regression techniques (including neural networks) that relates the battery's DOD, temperature, and age to a predicted strain response could be used in an anomaly detection algorithm for lithium-ion batteries. Rather than predicting DOD from strain measurements, the expected structural state of the battery can be predicted and used to assess its health and safety. Ultimately, the added cost of monitoring cell-casing strain has to be weighed against the many benefits provided by advanced, non-intrusive monitoring of the battery's internal state.

Acknowledgment

The authors would like to thank the more than 150 companies and organizations that support research activities at the Center for Advanced Life Cycle Engineering (CALCE) at the University of Maryland annually. The authors would also like to thank the members of the Prognostics and Health Management Consortium at CALCE and the National Science Foundation (Grant No. 1234451) for their support of this work. CEH would like to gratefully acknowledge the support provided by the ARCS Foundation.

Conflict of Interest

There are no conflicts of interest.

Data Availability Statement

The data sets generated and supporting the findings of this article are obtainable from the corresponding author upon reasonable request.

References

[1] Sonwane, A., Yuan, C., and Xu, J., 2021, "Coupling Effect of State-of-Charge and Strain Rate on the Mechanical Behavior of Electrodes of 21700 Lithium-Ion Battery," ASME J. Electrochem. Energy Convers. Storage, **18**(2), p. 020905.

[2] Wu, L., and Zhang, J., 2019, "Three-Dimensional Finite Element Study on Lithium Diffusion and Intercalation-Induced Stress in Polycrystalline $LiCoO_2$ Using Anisotropic Material Properties," ASME J. Electrochem. Energy Convers. Storage, **16**(2), p. 021008.

[3] Nguyen, T. D., Deng, J., Robert, B., Chen, W., and Siegmund, T., 2021, "Deformation Behavior of Single Prismatic Battery Cell Cases and Cell Assemblies Loaded by Internal Pressure," ASME J. Electrochem. Energy Convers. Storage, **18**(4), p. 040901.

[4] Reimers, J. N., and Dahn, J. R., 1992, "Electrochemical and In situ X-ray Diffraction Studies of Lithium Intercalation in Li_xCoO_2," J. Electrochem. Soc., **139**(8), pp. 2091–2097.

[5] Yin, R.-Z., Kim, Y.-S., Shin, S.-J., Jung, I., Kim, J.-S., and Jeong, S.-K., 2012, "In situ XRD Investigation and Thermal Properties of Mg Doped $LiCoO_2$ for Lithium Ion Batteries," J. Electrochem. Soc., **159**(3), pp. A253–A258.

[6] Padhi, K., Nanjundaswamy, K. S., and Goodenough, J. B., 1997, "Phospho-olivines as Positive-Electrode Materials for Rechargeable Lithium Batteries," J. Electrochem. Soc., **144**(2), pp. 1188–1194.

[7] Saïdi, M. Y., Barker, J., and Koksbang, R., 1996, "Structural and Electrochemical Investigation of Lithium Insertion in the Li_{1-X} Mn_2O_4 Spinel Phase," Electrochim. Acta, **41**(2), pp. 199–204.

[8] Dahn, J., Fong, R., and Spoon, M., 1990, "Suppression of Staging in Lithium-Intercalated Carbon by Disorder in the Host," Phys. Rev. B, **42**(10), pp. 6424–6432.

[9] Dahn, J., 1991, "Phase Diagram of Li_xC_6," Phys. Rev. B, **44**(17), pp. 9170–9177.

[10] Sethuraman, V. A., 2010, "Surface Structural Disordering in Graphite upon Lithium Intercalation/Deintercalation," J. Power Sources, **195**(11), pp. 3655–3660.

[11] Nadimpalli, S., Sethuraman, V., Abraham, D., Bower, A., and Guduru, P., 2015, "Stress Evolution in Lithium-Ion Composite Electrodes During Electrochemical Cycling and Resulting Internal Pressures on the Cell Casing," J. Electrochem. Soc., **162**(14), pp. A2656–A2663.

[12] Wang, X., Sone, Y., and Kuwajima, S., 2004, "In Situ Investigation of the Volume Change in Li-Ion Cell With Charging and Discharging," J. Electrochem. Soc., **151**(2), pp. A273–A280.

[13] Wang, X., Sone, Y., Segami, G., Naito, H., Yamada, C., and Kibe, K., 2007, "Understanding Volume Change in Lithium-Ion Cells During Charging and Discharging Using In Situ Measurements," J. Electrochem. Soc., **154**(1), pp. A14–A21.

[14] Mohan, S., Kim, Y., Siegel, J. B., Samad, N. A., and Stefanopoulou, A. G., 2014, "A Phenomenological Model of Bulk Force in a Li-Ion Battery Pack and its Application to State of Charge Estimation," J. Electrochem. Soc., **161**(14), pp. A2222–A2231.
[15] Gibellini, E., Lanciotti, C., Giovanardi, R., Bononi, M., Davolio, G., Marchetti, A., and Fontanesi, C., 2016, "Dimensional Changes in Automotive Pouch Li-Ion Cells: A Combined Thermo-mechanical/Electrochemical Study," J. Electrochem. Soc., **163**(10), pp. A2304–A2311.
[16] Oh, K.-Y., Epureanu, B. I., Siegel, J. B., and Stefanopoulou, A. G., 2016, "Phenomenological Force and Swelling Models for Rechargeable Lithium-Ion Battery Cells," J. Power Sources, **310**, pp. 118–129.
[17] Oh, K.-Y., Siegel, J. B., Secondo, L., Kim, S. U., Samad, N. A., Qin, J., Anderson, D., et al., 2014, "Rate Dependence of Swelling in Lithium-Ion Cells," J. Power Sources, **267**, pp. 197–202.
[18] Poloni, T., Figueroa-Santos, M. A., Siegel, J. B., and Stefanopoulou, A. G., "Integration of Non-monotonic Cell Swelling Characteristic for State-of-Charge Estimation," Proceedings of the 2018 Annual American Control Conference, Milwaukee, WI, June 27–29, 2018, pp. 2306–2311.
[19] Rieger, B., Erhard, S. V., Rumpf, K., and Jossen, A., 2016, "A New Method to Model the Thickness Change of a Commercial Pouch Cell During Discharge," J. Electrochem. Soc., **163**(8), pp. A1566–A1575.
[20] Rieger, B., Schlueter, S., Erhard, S. V., and Jossen, A., 2016, "Strain Propagation in Lithium-Ion Batteries From the Crystal Structure to the Electrode Level," J. Electrochem. Soc., **163**(8), pp. A1595–A1606.
[21] Schiffer, Z. J., Cannarella, J., and Arnold, C. B., 2016, "Strain Derivatives for Practical Charge Rate Characterization of Lithium-Ion Electrodes," J. Electrochem. Soc., **163**(3), pp. A427–A433.
[22] Lee, J. H., Lee, H. M., and Ahn, S., 2003, "Battery Dimensional Changes Occurring During Charge/Discharge Cycles—Thin Rectangular Lithium Ion and Polymer Cells," J. Power Sources, **119–121**, pp. 833–837.
[23] Fu, R., Xiao, M., and Choe, S.-Y., 2013, "Modeling, Validation and Analysis of Mechanical Stress Generation and Dimension Changes of a Pouch Type High Power Li-Ion Battery," J. Power Sources, **224**, pp. 211–224.
[24] Barker, J., 1999, "In-situ Measurement of the Thickness Changes Associated With Cycling of Prismatic Lithium Ion Batteries Based on $LiMn_2O_4$ and $LiCoO_2$," Electrochim. Acta, **45**(1–2), pp. 235–242.
[25] Sommer, L. W., Kiesel, P., Ganguli, A., Lochbaum, A., Saha, B., Schwartz, J., Bae, C.-J., Alamgir, M., and Raghavan, A., 2015, "Fast and Slow Ion Diffusion Processes in Lithium Ion Pouch Cells During Cycling Observed With Fiber Optic Strain Sensors," J. Power Sources, **296**, pp. 46–52.
[26] Sood, B. P., Pecht, M. G., and Osterman, M. D., 2018, Systems, Methods, and Devices for Health Monitoring of an Energy Storage Device, US Patent #US10014561B2.
[27] Sood, B., Hendricks, C., Osterman, M., and Pecht, M., 2014, "Health Monitoring of Lithium-Ion Batteries," Electron. Dev. Failure Anal., **16**(2), pp. 4–16.
[28] Wu, Y., Wang, Y., Yung, W. K. C., and Pecht, M., 2019, "Ultrasonic Health Monitoring of Lithium-Ion Batteries," Electronics, **8**(751), pp. 1–16.
[29] Yu, X., Feng, Z., Ren, Y., Henn, D., Wu, Z., An, K., Wu, B., Fau, C., Li, C., and Harris, S. J., 2018, "Simultaneous Operando Measurements of the Local Temperature, State of Charge, and Strain Inside a Commercial Lithium-Ion Battery Pouch Cell," J. Electrochem. Soc., **165**(7), pp. A1578–A1585.
[30] Zhao, Y., Spingler, F. B., Patel, Y., Offer, G. J., and Jossen, A., 2019, "Localized Swelling Inhomogeneity Detection in Lithium-Ion Cells Using Multi-dimensional Laser Scanning," J. Electrochem. Soc., **166**(2), pp. A27–A34.
[31] Hendricks, C., Williard, N., Mathew, S., and Pecht, M., 2015, "A Failure Modes, Mechanisms, and Effects Analysis (FMMEA) of Lithium-Ion Batteries," J. Power Sources, **297**, pp. 113–120.
[32] Zhang, J., and Lee, J., 2011, "A Review on Prognostics and Health Monitoring of Li-Ion Battery," J. Power Sources, **196**(15), pp. 6007–6014.
[33] Piller, S., Perrin, M., and Jossen, A., 2001, "Methods for State of Charge Determination and Their Applications," J. Power Sources, **96**(1), pp. 113–120.
[34] Saha, B., Goebel, K., and Christophersen, J., 2009, "Comparison of Prognostic Algorithms for Estimating Remaining Useful Life of Batteries," Trans. Inst. Meas. Control, **31**(3–4), pp. 293–308.
[35] Ng, K. S., Moo, C.-S., Chen, Y.-P., and Hsieh, Y.-C., 2009, "Enhanced Coulomb Counting Method for Estimating State of Charge and State of Health of Lithium-Ion Batteries," Appl. Energy, **86**(9), pp. 1506–1511.
[36] Waag, W., Fleischer, C., and Sauer, D. U., 2014, "Critical Review of the Methods for Monitoring of Lithium-Ion Batteries in Electric and Hybrid Vehicles," J. Power Sources, **258**, pp. 321–339.
[37] Aylor, J., 1992, "Battery State of Charge Indicator for Electric Wheelchairs," IEEE Trans. Ind. Electron., **39**(5), pp. 398–409.
[38] Plett, G., 2004, "Extended Kalman Filtering for Battery Management Systems of LiPB-Based HEV Battery Packs. Part 2: Modeling and Identification," J. Power Sources, **134**(2), pp. 262–276.
[39] Li, J., Klee Barillas, J., Guenther, C., and Danzer, M. A., 2013, "A Comparative Study of State of Charge Estimation Algorithms for $LiFePO_4$ Batteries Used in Electric Vehicles," J. Power Sources, **230**, pp. 244–250.
[40] Charkhgard, M., and Farrokhi, M., 2010, "State of Charge Estimation for Lithium-Ion Batteries Using Neural Networks and EKF," IEEE Trans. Ind. Electron., **57**(12), pp. 4178–4187.
[41] Cho, S., Jeong, H., Han, C., Jin, S., Lim, J. H., and Oh, J., 2012, "State-of-Charge Estimation for Lithium-Ion Batteries Under Various Operating Conditions Using an Equivalent Circuit Model," Comput. Chem. Eng., **41**, pp. 1–9.
[42] He, W., Williard, N., Chen, C., and Pecht, M., 2014, "State of Charge Estimation for Li-Ion Batteries Using Neural Network and Unscented Kalman-Based Error Correction," Electr. Power Energy Syst., **62**, pp. 783–791.